Properties of AGN coronae in the *NuSTAR* era

A. C. Fabian,[1][*] A. Lohfink,[1] E. Kara,[1] M. L. Parker,[1] R. Vasudevan[1]
and C. S. Reynolds[1,2]

[1]*Institute of Astronomy, Madingley Road, Cambridge CB3 0HA, UK*
[2]*Department of Astronomy, University of Maryland, College Park, MD 20742-2421, USA*

ABSTRACT

The focusing optics of *NuSTAR* have enabled high signal-to-noise ratio spectra to be obtained from many X-ray bright active galactic nuclei (AGN) and galactic black hole binaries (BHB). Spectral modelling then allows robust characterization of the spectral index and upper energy cutoff of the coronal power-law continuum, after accounting for reflection and absorption effects. Spectral-timing studies, such as reverberation and broad iron line fitting, of these sources yield coronal sizes, often showing them to be small and in the range of 3 to 10 gravitational radii in size. Our results indicate that coronae are hot and radiatively compact, lying close to the boundary of the region in the compactness–temperature ($\Theta - \ell$) diagram which is forbidden due to runaway pair production. The coincidence suggests that pair production and annihilation are essential ingredients in the coronae of AGN and BHB and that they control the shape of the observed spectra.

Key words: accretion, accretion discs – black hole physics – X-rays: binaries – X-rays: galaxies.

1 INTRODUCTION

The variable hard X-ray emission from active galactic nuclei (AGN) is generally considered to originate in a compact region known as the corona which lies above the accretion disc (see e.g. Vaiana & Rosner 1978; Haardt & Maraschi 1993; Merloni & Fabian 2003). The inner accretion disc produces copious UV emission in a quasi-blackbody spectral shape which is Compton upscattered by hot coronal electrons energized by magnetic fields from the disc. Rapid variability of the 2–10 keV X-ray emission seen from many AGN indicates that the corona is physically small. Recent X-ray spectral-timing and reverberation analyses of AGN spectra strongly support this conclusion and in many cases require the corona to lie just $3-10r_\mathrm{g}$ above the central black hole (Fabian et al. 2009; De Marco et al. 2011; Kara et al. 2013; Cackett et al. 2014; Emmanoulopoulos et al. 2014; Uttley et al. 2014). Variability analyses of microlensed components of several lensed quasars also indicate small hard X-ray emission regions, with half-light radii less than $6r_\mathrm{g}$. Together, the evidence points to the corona being compact (Fabian 2012; Reis & Miller 2013). Further evidence of a small physical size of the corona emerges from observations of the emissivity profile of the broad iron line (Wilkins & Fabian 2011) and from varying obscuration of the corona by clouds (Risaliti et al. 2011; Sanfrutos et al. 2013).

Sources which are physically small and highly luminous can also be compact in a radiative sense, meaning that interactions involving significant energy exchange between photons and particles are commonplace in the source. The relevant parameter here is then the ratio of source luminosity to size (L/R: Cavaliere & Morrison 1980), usually given in terms of the dimensionless compactness parameter (Guilbert, Fabian & Rees 1983, hereafter GFR):

$$\ell = \frac{L}{R} \frac{\sigma_\mathrm{T}}{m_\mathrm{e} c^3}, \tag{1}$$

where L is the luminosity, R the radius of the source (assumed spherical), σ_T the Thomson cross-section and m_e the mass of the electron. When $\ell \sim 1$ a particle loses a significant fraction of its energy on crossing the source region (see Section 2).

An idea of the magnitude of ℓ can be seen by replacing R by R_g, the gravitational radius (GM/c^2), and comparing the luminosity L with the Eddington limit L_E,

$$\ell = 4\pi \frac{m_\mathrm{p}}{m_\mathrm{e}} \frac{R_\mathrm{g}}{R} \frac{L}{L_\mathrm{E}}. \tag{2}$$

Thus sources operating with coronal emission exceeding 1 per cent of the Eddington limit with coronae which are less than $\sim 20r_\mathrm{g}$ in size are compact in the sense that $\ell > 10$.

If the photons are energetic enough, photon–photon collisions can lead to pair production which can play a major role in determining the outgoing spectrum and overall composition of the corona (Svensson 1982, 1984; Zdziarski 1985; GFR). Consider a small region of size R containing soft photons and unit Thomson depth of electrons (i.e. $\tau_\mathrm{T} = n_\mathrm{e} \sigma_\mathrm{T} R = 1$) into which an increasing amount of power is fed into the electrons. As the electron

temperature $\Theta = kT_e/m_e c^2$ rises, Compton scattering of the soft photons produces a power-law radiation spectrum extending to a Wien tail at energies around 2Θ. Photon–photon collisions create electron–positron pairs when the product of the photon energies, in units of $m_e c^2$, exceeds 2. Thus pairs appear when the tail extends above $\sim 2m_e c^2$ (i.e. 1 MeV). The pair density is proportional to the luminosity and temperature and inversely proportional to the source size. The energy associated with increased luminosity goes into increased numbers of pairs rather than temperature. Pair production can become a runaway process, outstripping annihilation, soaking up energy and limiting any rise in temperature.[1] When the source is radiatively compact this happens at $\Theta < 0.2$ ($kT_e < 100$ keV).

Photon–photon collisions involving hard X-rays can thus produce electron–positron pairs which act as an ℓ-dependent thermostat (Svensson 1984; Zdziarski 1985; Pietrini & Krolik 1995; Stern et al. 1995; Coppi 1999; Dove et al. 1997). This limits the source temperature $\Theta = kT_e/m_e c^2$ as a function of ℓ. The only other major factor here is the source geometry and its location with respect to the soft photon source.

It has been suspected for over 30 years that luminous AGN and black hole binary (BHB) sources such as Cygnus X-1 are radiatively compact. Done & Fabian (1989) tabulate compactness parameters of several dozen AGN based on their observed X-ray luminosity and an estimate/limit of source size, obtained from rapid variability. They found many sources with $1 < \ell < 100$. However, robust estimates of the coronal temperature and in particular the size of the corona have however been lacking. Now, however, with spectral timing results combined with temperature estimates becoming available from *NuSTAR*, robust values of both ℓ and Θ can be obtained, after carefully accounting for disc reflection in the spectrum. *NuSTAR* is the first telescope for cosmic X-ray sources with focusing optics operating in hard X-rays up to 78 keV. This means that it yields high signal-to-noise ratio spectra over the band where the corona emits most of its power.

In this paper we gather results from *NuSTAR* and from the coded mask instruments Integral and *Swift*-BAT on AGN and BHB to map out their locations on the ℓ–Θ diagram. High power levels fed into a compact corona should produce a spectrum (e.g. photon index and high-energy turnover) constrained by source size, luminosity and geometry. Observations of source size and luminosity can in principle therefore enable us to establish the geometry of the corona and reveal the heating and thermalization mechanisms operating.

Note that we only consider coronae where emission is generated, not the large scattering corona in the low-mass X-ray binaries known as Accretion Disc Corona sources (e.g. Church & Balucinska-Church 2004).

2 THE $\Theta - \ell$ PLANE

We begin by gathering together various theoretical constraints from GFR, Svensson (1984), and Fabian (1994) within the temperature–compactness, $\Theta - \ell$, plane. The estimates are initially deduced for non-relativistic temperatures, but the coupling times are extended into the transrelativistic regime using the work of Ghisellini, Haardt & Fabian (1993, hereafter GHF).

---

[1] The existence of a temperature limit due to pair production by particle collisions in a low-density plasma was first shown by Bisnovatyi-Kogan, Zeldovich & Sunyaev (1971).

Consider a spherical source of size R and scattering optical depth τ in which luminosity L is generated. The energy density in photons is then

$$\varepsilon = \frac{L}{4\pi R^2 c}(1 + \tau) \tag{3}$$

and thus the Compton cooling time of an electron is

$$t_C = \frac{3\pi R}{2c\ell(1 + \tau)}. \tag{4}$$

Expressed in terms of the light crossing time of the source, t_{cross},

$$\frac{t_C}{t_{cross}} = \frac{3\pi}{2\ell(1 + \tau)}. \tag{5}$$

If $\ell > 2$ then we have $t_C < t_{cross}$. This justifies the statement made in the Introduction that, when ℓ exceeds unity, an electron loses much of its energy on crossing the source.

The dominant radiation process will be the one with the shortest cooling time. The bremsstrahlung cooling time of an electron in a gas of density n is

$$t_B = \frac{\Theta^{\frac{1}{2}}}{n\alpha_f \sigma_T c} = \frac{\Theta^{\frac{1}{2}} R}{\tau \alpha_f c}, \tag{6}$$

where α_f is the fine-structure constant, which we compare with t_C, to give

$$\ell = \frac{3\pi\alpha_f}{2\Theta^{\frac{1}{2}}} \frac{\tau}{1 + \tau} \tag{7}$$

and an upper limit to bremsstrahlung dominance when

$$\ell \approx 3\alpha_f \Theta^{-\frac{1}{2}}. \tag{8}$$

This demonstrates that Comptonization dominates at high compactness.

Two-body collisions are the simplest heating and thermalization mechanism, with electron–proton coupling occurring faster than electron cooling when

$$\ell < 0.04\Theta^{-3/2}; \tag{9}$$

the relevant relation for electron–electron coupling is

$$\ell < 80\Theta^{-3/2} \tag{10}$$

(Fabian 1994). Both of these relations are non-relativistic and apply only at low electron temperatures ($\Theta < <1$): in Fig. 1, we plot the electron–proton and electron–electron coupling lines from GHF, which have been calculated through the transrelativistic regime.

Pair production at high ℓ values is dominated by photon–photon collisions. An estimation of the pair density requires a detailed calculation covering pair production and annihilation and also the thermal balance. Above a certain level, which we call the pair line, pair production runs away, as described in the Introduction. Svensson (1984) estimated that, for an isolated cloud, the pair balance line occurs where

$$\ell \sim 10\Theta^{5/2} \exp(1/\Theta). \tag{11}$$

The position of the pair line depends on the geometry of the region and the origin and level of the dominant soft photon field. Stern et al. (1995) computed the pair balance curve for a slab corona above a reflecting disc and obtained the line included in Fig. 1. They also computed the constraints for a hemispherical corona on a slab and a sphere at a height equal to half the radius of the sphere (see Svensson 1996).
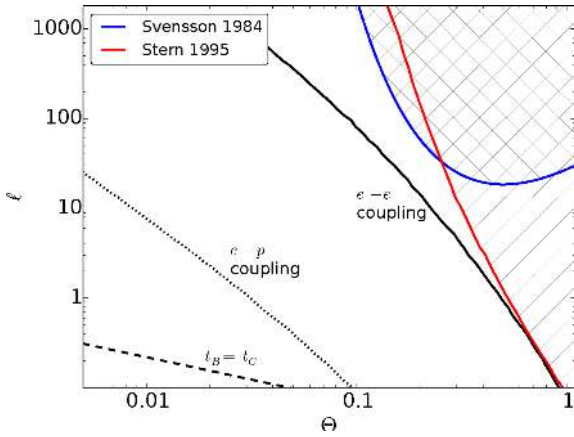
Figure 1. Summary of our theoretical understanding of the $\Theta - \ell$ plane as described in detail in Section 2; included are the boundaries for electron–electron coupling, electron–proton coupling, the dominance of Compton cooling and pair lines for different assumptions.

3 THE LOCATION OF OBSERVED SOURCES ON THE $\Theta - \ell$ PLANE

In the last section we have seen what physical processes govern the placement of observations in the $\Theta - \ell$ plane. This section concerns the collection and analysis of the data used to populate the observational $\Theta - \ell$ plane presented in this paper.

3.1 From observations to the $\Theta - \ell$ plane

To construct our observational $\Theta - \ell$ plane, the coronal temperature (kT_e) is estimated throughout this work from the high-energy cut-off

$[M(E) \sim E^{-\Gamma} \exp(-E/E_{\text{cut}})]$. To convert from the cut-off energy to the coronal temperature a factor of 2 is used ($kT_e = E_{\text{cut}}/2$). As discussed in Petrucci et al. (2001) a conversion factor of 2 is appropriate for optical depths smaller than one; if the optical depth is much larger than 1, the factor is closer to 3. We account for the uncertainty of the conversion in the errors on Θ in addition to the statistical uncertainty. For determining luminosities, the flux of the power-law component in the 0.1–200 keV band is estimated and converted using a value of 68 km s^{-1} Mpc^{-1} is used for the Hubble constant.

3.2 Sample selection and data collection

The data we will consider is divided into two categories; the first is where the information on the high-energy cut-off is from a *NuSTAR* observation (CAT 1) and the second is where the information on the high-energy cut-off is from the BAT instrument onboard *Swift* (CAT 2). Finally, we include results obtained from microlensed quasars observed with *Chandra* in the second category.

In our CAT 1 sample we include all those sources which have work which is published or in preparation that provide a constraint on the high-energy cut-off from *NuSTAR*, even if it is only a lower limit. The so-selected CAT 1 targets are shown, together with the measurements of our observables, in Tables 1 and 2 for AGN and BHB, respectively. (Most of the BHB are in the hard state.) As *NuSTAR* provides spectra with the best signal-to-noise ratio in the hard X-ray band and modelling usually includes detailed fitting of any reflection components, we expect *NuSTAR* spectra to provide the most robust results.

The values for the high-energy cut-offs of the CAT 1 sample stem from the individual works quoted in the right-most column

Table 1. The targets and properties of the AGN with cut-off constraints resulting from observations with *NuSTAR*. The references to the individual works are given in the right-most column.

Source	z	$\log(M)$ ($M_\odot$)	r_{co} (r_G)	F_x	E_{cut} (keV)	Γ	Θ	ℓ	Data	References
NGC 5506	0.006	8 ± 1	10	2.9	720^{+130}_{-190}	$1.91^{+0.03}_{-0.03}$	$0.71^{+0.13}_{-0.36}$	4^{+33}_{-3}	SWIFT/NU	1, 2
NGC 7213	0.006	$7.98^{+0.22}_{-0.24}$	10	0.71	>240	$1.84^{+0.03}_{-0.03}$	>0.05	$1.0^{+0.7}_{-0.4}$	NU	3, 4
MCG-6-30-15	0.008	6.7 ± 1	2.9	8.2	>110	$2.061^{+0.005}_{-0.005}$	>0.04	258^{+2323}_{-232}	XMM/NU	5, 6
NGC 2110	0.008	8.3 ± 1	10	8.9	>210	$1.64^{+0.03}_{-0.03}$	>0.07	10^{+89}_{-9}	SWIFT/NU	7, 8
MCG 5-23-16	0.009	7.85 ± 1	10	4.2	116^{+6}_{-5}	$1.85^{+0.01}_{-0.01}$	$0.11^{+0.01}_{-0.04}$	15^{+136}_{-14}	NU	9–11
SWIFT J2127.4+5654	0.014	7.18 ± 1	13	1.1	108^{+11}_{-10}	$2.08^{+0.01}_{-0.01}$	$0.11^{+0.01}_{-0.04}$	34^{+308}_{-31}	XMM/NU	12, 13
IC4329A	0.016	8.1 ± 1	10	4.9	186^{+14}_{-14}	$1.73^{+0.01}_{-0.01}$	$0.18^{+0.01}_{-0.07}$	41^{+365}_{-37}	SU/NU	14, 15
NGC 5548	0.018	$7.59^{+0.24}_{-0.21}$	4.5	1.3	70^{+40}_{-10}	$1.49^{+0.05}_{-0.05}$	$0.07^{+0.04}_{-0.03}$	88^{+55}_{-37}	XMM/NU	5,16,17
Mrk 335	0.026	$7.42^{+0.12}_{-0.16}$	3	0.10	>174	$2.14^{+0.02}_{-0.04}$	>0.06	36^{+16}_{-9}	SWIFT/NU	18, 19
Ark 120	0.033	$7.66^{+0.05}_{-0.06}$	4.4	0.55	>68	$1.73^{+0.02}_{-0.02}$	>0.06	4^{+1}_{-1}	XMM/NU	20, 21
1H0707−495	0.041	6.31 ± 1	2	0.14	>63	$3.2^{+0.2}_{-0.2}$	>0.02	358^{+3219}_{-322}	SWIFT/NU	22, 23
Fairall 9	0.047	$8.41^{+0.11}_{-0.09}$	21	0.87	>242	$1.96^{+0.01}_{-0.02}$	>0.08	12^{+3}_{-3}	XMM/NU	20, 24
3C 390.3	0.056	$9.40^{+0.05}_{-0.06}$	10	1.6	116^{+24}_{-8}	$1.70^{+0.01}_{-0.01}$	$0.11^{+0.02}_{-0.04}$	18^{+3}_{-2}	SU/NU	25, 26
Cyg A	0.056	$9.40^{+0.11}_{-0.14}$	10	1.1	>110	$1.47^{+0.13}_{-0.06}$	>0.04	6^{+2}_{-1}	NU	27, 28
3C 382	0.058	9.2 ± 0.5	10	1.4	214^{+147}_{-63}	$1.68^{+0.03}_{-0.02}$	$0.21^{+0.14}_{-0.11}$	12^{+25}_{-8}	SWIFT/NU	29, 30

F_x is the 0.1–200 keV X-ray flux in 10^{-10} erg cm^{-2} s^{-1}.

References: 1: Guainazzi et al. (2010), 2: Matt et al. (2015), 3: Ursini et al. (2015b), 4: Blank, Harnett & Jones (2005), 5: Emmanoulopoulos et al. (2014), 6: Marinucci et al. (2014c), 7: Moran et al. (2007), 8: Marinucci et al. (2014a), 9: Ponti et al. (2012), 10: Zoghbi et al. (2014), 11: Baloković et al. (2015), 12: Malizia et al. (2008), 13: Marinucci et al. (2014b), 14: Bianchi et al. (2009), 15: Brenneman et al. (2014), 16: Pancoast et al. (2014), 17: Ursini et al. (2015a), 18: Grier et al. (2012), 19: Parker et al. (2014), 20: Peterson et al. (2004), 21: Matt et al. (2014), 22: Bian & Zhao (2003), 23: Kara et al. (2015), 24: Lohfink & Reynolds (in preparation), 25: Grier et al. (2013), 26: Lohfink & Tombesi (in preparation), 27: Tadhunter et al. (2003), 28: Reynolds et al. (2015), 29: Winter et al. (2009), 30: Ballantyne et al. (2014).

Table 2. The targets and properties of the black hole X-ray binaries with cut-off constraints resulting from observations with *NuSTAR*. The references to the individual works are given in the right-most column.

Source	d (kpc)	M ($M_\odot$)	r_{co} (r_G)	F_x	E_{cut} (keV)	Γ	Θ	ℓ	Data	References
GRS 1739−278	8.5	10 ± 5	5	1.1	$31.3^{+0.3}_{-0.3}$	1.44 ± 0.01	$0.0306^{+0.0003}_{-0.0104}$	349^{+349}_{-116}	NU	1–3
GRS 1915+105	11.0	10.1 ± 0.6	10	2.9	$35.6^{+0.3}_{-0.3}$	1.72 ± 0.02	$0.0348^{+0.0003}_{-0.0118}$	751^{+47}_{-42}	NU	4, 5
GX 339-4	8.0	10 ± 5	150	0.36	>370	1.60 ± 0.03	>0.12	3^{+3}_{-1}	XMM/NU	6, 7
Cyg X-1 soft	1.86	14.8 ± 1.0	10	6.1	120^{+20}_{-10}	$2.59^{+0.01}_{-0.02}$	$0.12^{+0.02}_{-0.05}$	32^{+2}_{-2}	SU/NU	8–10
Cyg X-1 hard	1.86	14.8 ± 1.0	3.3	3.0	156 ± 3	1.568 ± 0.005	$0.153^{+0.003}_{-0.053}$	47^{+3}_{-3}	SU/NU	8, 9,12

F_x is the 0.1–200 keV X-ray flux in 10^{-8} erg cm^{-2} s^{-1}.

References: 1: Dennerl & Greiner (1996), 2: Greiner, Dennerl & Predehl (1996), 3: Miller et al. (2015), 4: Miller et al. (2013), 5: Steeghs et al. (2013), 6: Zdziarski et al. (2004), 7: Fuerst & Al. (2015), 8: Orosz et al. (2011), 9: Reid et al. (2011), 10: Tomsick et al. (2014), 11: Parker et al. (2015).

of the tables. If more than one epoch of observations exists we select the one with the best constraint on the cut-off. The estimates on the coronal size originate from modelling of the reflection spectrum and X-ray reverberation measurements (unless the source is lensed). If no measurement exists we assume a value of $10\,R_g$ which is a conservative assumption given the measurements. For the black hole masses required to derive the actual size of the coronal region, we use optical broad line reverberation measurements where they are available. If the mass estimate in the literature does not have an error estimate we assume a conservative uncertainty of a factor of 10 for AGN. For Galactic BHB we assume a black hole mass of $10 \pm 5\,M_\odot$ if no mass estimate exists. For sources observed with *NuSTAR*, we estimate the coronal luminosities from the coronal fluxes of the best-fitting spectral models presented in the individual works. To do this we use a cut-off power law with their best-fitting Γ, E_{cut}, and power-law normalization, if given. If no power-law normalization is given we determine it from the flux measurement of the most power-law-dominated band, given in the paper. The coronal flux is then determined in the energy range 0.1–200 keV, as below this band the spectrum could deviate significantly from a power law and most sources already roll-over below 200 keV. In case of the X-ray binaries we then use the distance to get the luminosity and for AGNs we use the redshifts, which are drawn from the NASA/IPAC Extragalactic Database (NED).

Our CAT 2 sample is assembled from three works; an analysis of XMM/INTEGRAL/BAT Type 1 AGN observations by Malizia et al. (2014), an analysis of XMM/BAT AGN observations in the Northern Galactic Cap by Vasudevan et al. (2013) and a microlensing sample presented in Chen et al. (2012). In the first case the BAT spectra are those of the 70 month catalogue, and in the second case those of the 58 month catalogue. We select from the first two samples subsamples of sources with mass estimates and constraints on the high-energy cut-off. For the microlensing sample we use sources where an estimate of the coronal size exists. The selected sources and measurements are listed in Tables 3–5.

The assumptions made for the coronal temperatures, coronal size and black hole mass are the same as for the CAT 1 sample. The coronal fluxes for the Vasudevan et al. (2013) sources are also determined in a similar fashion to what was described above. For the Malizia et al. (2014) sample the same method cannot be applied as no flux values are given in the paper, instead we use the best-fitting BAT cross-calibration constant. We downloaded the 70 month BAT spectra of the sources and set up a spectral model consisting of a cut-off power law multiplied by the cross-calibration constant. The photon index, high-energy cut-off and cross-calibration constant are

kept fixed at their best-fitting values, while we fit for the normalization. Once the best-fitting normalization is found we delete the constant and estimate the coronal flux in the 0.1–200 keV just as before. Again, the redshifts from NED are used to obtain the coronal luminosity. The microlensed sample is treated differently as the measurement of the physical size of the X-ray emitting region is already non-dimensionless and can be used to calculate ℓ directly, the black hole mass is therefore not required. We assume further the highest energy bin in the *Chandra* spectra shown in Chen et al. (2012) is a lower limit on the high-energy cut-off. This is them corrected for redshift. Finally, for the coronal luminosities of the lensed quasars we use the 0.2–50 keV luminosities reported in the Chen et al. (2012) paper. These objects serve to show that distant quasars operate at values of ℓ within the range 10–100 or greater; NuSTAR observations will be required to measure their expected cutoffs and thus Θ values.

4 RESULTS

The results for the *NuSTAR* sample (CAT1) are plotted in Fig. 2. Although some of the results are lower limits, about one half are measurements of clear turnovers seen in the *NuSTAR* band. A few examples of AGN with clear turnovers are MCG-5-23-16 and SWIFT J2127.4+5654, while examples of BHB are GRS 1915+105, GRS 1739−278 and Cyg X-1. The largest cutoff energy is inferred in the AGN NGC 5506, which is at low ℓ.

Several factors can affect the measurement of coronal temperature. The first is observational and due to the common usage of an exponential cutoff as a model for the upper spectral turnover produced by Comptonization. As shown by Zdziarski et al. (2003), this produces a slower break than Comptonization, which retains a straight power-law shape to higher energies before more abruptly turning down. We have simulated this by generating Comptonization spectra using COMPPS (Poutanen, Nagendra & Svensson 1996) in a spherical geometry for a seed photon temperature of 10 eV, a Thomson depth $\tau = 1$ and a set of temperatures (40 keV, 60 keV, 70 keV, 80 keV, 90 keV, 100 keV, 120 keV, 150 keV, 200 keV) (Fig. 3). These have been fitted with a power law in the 0.5–10 keV band and the power law was later modified at higher energies using an exponential turnover assumed to represent the effect of a turnover at $2\,kT_e$. The plot demonstrates that when the temperature is significantly above the *NuSTAR* band (i.e. $\Theta > 0.2$) and no significant deviation is yet seen in the *NuSTAR* spectrum, then it is possible that the cutoff energy and thus temperature are overestimated. These effects have been carefully considered by Matt et al. (2015) in their study of

Table 3. The targets and properties of the AGN analysed by Malizia et al. (2014) included in this work. The reference to the works providing the mass estimates are given in the right-most column.

Source	z	$\log(M)$ $(M_\odot)$	r_{co} (r_G)	F_x	E_{cut} (keV)	Γ	Θ	ℓ	Data	References
IGR J0033+6122	0.105	8.5 ± 0.5	10	3.2	>52	$1.50^{+0.32}_{-0.09}$	>0.02	481^{+1041}_{-329}	XMM/INT/BAT	1
3C 111	0.049	9.6 ± 0.8	10	5.4	136^{+47}_{-29}	$1.65^{+0.04}_{-0.02}$	$0.13^{+0.05}_{-0.06}$	14^{+73}_{-12}	XMM/INT/BAT	2
MCG+08-11-011	0.021	8.1 ± 0.6	10	5.1	171^{+44}_{-30}	1.79 ± 0.01	$0.17^{+0.04}_{-0.07}$	73^{+219}_{-55}	XMM/INT/BAT	2
Mrk 6	0.019	8.2 ± 0.5	10	0.94	131^{+132}_{-48}	$1.53^{+0.14}_{-0.13}$	$0.13^{+0.13}_{-0.07}$	9^{+19}_{-6}	XMM/INT/BAT	3
IGR J07597−3842	0.040	8.3 ± 0.5	10	1.0	79^{+24}_{-16}	1.58 ± 0.04	$0.08^{+0.02}_{-0.04}$	36^{+77}_{-24}	XMM/INT/BAT	4
NGC 3783	0.010	$7.47^{+0.007}_{-0.009}$	10	5.6	98^{+79}_{-34}	1.75 ± 0.09	$0.10^{+0.08}_{-0.05}$	76^{+2}_{-1}	XMM/INT/BAT	5
NGC 4151	0.003	$7.5^{+0.1}_{-0.6}$	10	22	196^{+47}_{-32}	1.63 ± 0.04	$0.19^{+0.05}_{-0.09}$	33^{+97}_{-7}	XMM/INT/BAT	6
IGR J12415−5750	0.024	8.0 ± 0.5	10	0.64	175^{+296}_{-74}	$1.53^{+0.04}_{-0.03}$	$0.17^{+0.29}_{-0.11}$	16^{+35}_{-11}	XMM/INT/BAT	1
MCG-06-30-15	0.008	$6.7^{+0.1}_{-0.2}$	2.9	2.1	63^{+24}_{-14}	$1.97^{+0.09}_{-0.03}$	$0.06^{+0.02}_{-0.03}$	105^{+62}_{-22}	XMM/INT/BAT	7, 8
IC4329A	0.016	7 ± 1	10	7.7	152^{+51}_{-32}	1.81 ± 0.03	$0.15^{+0.05}_{-0.07}$	856^{+7701}_{-770}	XMM/INT/BAT	5
IGR J16558−5203	0.054	7.9 ± 0.5	10	0.91	194^{+202}_{-72}	1.71f	$0.19^{+0.20}_{-0.11}$	142^{+308}_{-97}	XMM/INT/BAT	4
GRS 1734−292	0.021	8.9 ± 0.7	10	2.1	58^{+24}_{-7}	$1.55^{+0.15}_{-0.08}$	$0.06^{+0.02}_{-0.02}$	5^{+20}_{-4}	XMM/INT/BAT	9
3C 390.3	0.056	$8.46^{+0.009}_{-0.1}$	10	1.5	97^{+20}_{-11}	$1.56^{+0.03}_{-0.03}$	$0.10^{+0.02}_{-0.04}$	68^{+18}_{-1}	XMM/INT/BAT	5
NGC 6814	0.005	7.1 ± 0.2	10	1.3	190^{+185}_{-66}	1.68 ± 0.02	$0.19^{+0.18}_{-0.11}$	12^{+7}_{-5}	XMM/INT/BAT	6
4C 74.24	0.104	9.6 ± 0.5	10	0.41	189^{+171}_{-66}	1.82 ± 0.02	$0.19^{+0.17}_{-0.11}$	5^{+10}_{-3}	XMM/INT/BAT	10
S5 2116+81	0.086	8.8 ± 0.5	10	0.68	>180	1.90 ± 0.04	>0.06	34^{+74}_{-23}	XMM/INT/BAT	3
1H2251−179	0.064	6.9 ± 1.0	10	2.01	138^{+38}_{-57}	$1.67^{+0.08}_{-0.08}$	$0.14^{+0.04}_{-0.08}$	4437^{+39936}_{-3994}	XMM/INT/BAT	2
MCG-02-58-022	0.047	7.1 ± 0.6	10	1.8	>510	$1.95^{+0.03}_{-0.04}$	>0.17	1360^{+4054}_{-1018}	XMM/INT/BAT	2

F_x is the 0.1–200 keV X-ray flux in 10^{-10} erg cm^{-2} s^{-1}.
References: 1: Masetti et al. (2009), 2: Middleton, Done & Schurch (2007), 3: Winter et al. (2009), 4: Masetti et al. (2006), 5: Peterson et al. (2004), 6: Hicks & Malkan (2008), 7: Uttley & McHardy (2005), 8: Emmanoulopoulos et al. (2014), 9: Beckmann et al. (2009), 10: Woo & Urry (2002).

Table 4. The targets and properties of the AGN analysed by Vasudevan et al. (2013) included in this work. The reference to the works providing the mass estimates are given in the right-most column.

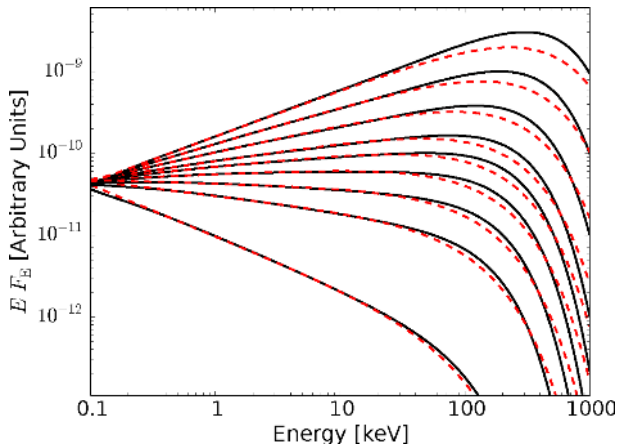| Source	z	$\log(M)$ $(M_\odot)$	r_{co} (r_G)	F_x	E_{cut} (keV)	Γ	Θ	ℓ	Data	References
NGC 3227	0.004	$6.78^{+0.08}_{-0.11}$	10	0.28E	>636	$2.08^{+0.05}_{-0.09}$	>0.21	3^{+1}_{-1}	XMM/BAT	1[b]
PG 1114+445	0.144	8.4 ± 1	10	0.080	69_{-47}	$1.60^{+0.60}_{-0.22}$	$0.07_{-0.05}$	27^{+245}_{-25}	XMM/BAT	2
NGC 4051	0.002	$6.13^{+0.12}_{-0.16}$	10	0.15	>381	$2.49^{+0.11}_{-0.12}$	>0.12	3^{+1}_{-1}	XMM/BAT	3[b]
PG 1202+281	0.165	8.5 ± 1	10	0.11	556_{-492}	$2.08^{+0.17}_{-0.16}$	>0.50	46^{+414}_{-41}	XMM/BAT	2
NGC 4138	0.003	$6.8^{+0.5}_{-0.5}$	10	0.46	148_{-73}	$1.51^{+0.34}_{-0.20}$	$0.15_{-0.10}$	3^{+6}_{-2}	XMM/BAT	4
NGC 4151	0.003	$7.56^{+0.05}_{-0.05}$	10	1.9	79^{+4}_{-4}	$1.31^{+0.03}_{-0.03}$	$0.077^{+0.003}_{-0.028}$	$2.5^{+0.3}_{-0.3}$	XMM/BAT	5, 7
Mrk 766	0.013	$6.82^{+0.05}_{-0.06}$	3.4	0.12	21^{+7}_{-6}	$1.56^{+0.09}_{-0.08}$	$0.021^{+0.007}_{-0.011}$	13^{+2}_{-1}	XMM/BAT	8–10
NGC 4258	0.002	$7.59^{+0.01}_{-0.01}$	10	0.59	>284	$1.82^{+0.06}_{-0.10}$	>0.09	$0.145^{+0.003}_{-0.003}$	XMM/BAT	11
Mrk 50	0.023	$7.42^{+0.06}_{-0.07}$	10	0.52	>334	$2.18^{+0.02}_{-0.02}$	>0.11	46^{+8}_{-6}	XMM/BAT	12
NGC 4388	0.008	$7.2^{+0.6}_{-0.6}$	10	0.14	>2096	$1.81^{+0.03}_{-0.05}$	>0.68	26^{+78}_{-20}	XMM/BAT	13
NGC 4395	0.001	$5.45^{+0.13}_{-0.15}$	51.5	0.20	45^{+27}_{-10}	$1.18^{+0.11}_{-0.12}$	$0.04^{+0.03}_{-0.02}$	3^{+1}_{-1}	XMM/BAT	10,14
NGC 4593	0.009	$6.88^{+0.08}_{-0.10}$	10	1.7	>517	$1.89^{+0.08}_{-0.05}$	>0.17	76^{+21}_{-13}	XMM/BAT	15, 16
NGC 5252	0.023	$9.03^{+0.40}_{-0.02}$	10	0.50	111^{+58}_{-18}	$1.38^{+0.09}_{-0.05}$	$0.11^{+0.06}_{-0.05}$	$1.1^{+0.1}_{-0.6}$	XMM/BAT	17
NGC 5506	0.006	6.7 ± 0.7	10	3.2	166^{+107}_{-30}	$1.85^{+0.02}_{-0.10}$	$0.16^{+0.11}_{-0.07}$	104^{+417}_{-83}	XMM/BAT	13
NGC 5548	0.017	$7.59^{+0.24}_{-0.21}$	4.5	1.8	415^{+827}_{-178}	$1.73^{+0.02}_{-0.02}$	$0.41^{+0.81}_{-0.25}$	59^{+37}_{-25}	XMM/BAT	10,18
Mrk 1383	0.087	$9.00^{+0.11}_{-0.16}$	10	0.36	>134	$2.20^{+0.24}_{-0.20}$	>0.04	11^{+5}_{-2}	XMM/BAT	5
Mrk 817	0.031	$7.59^{+0.07}_{-0.06}$	10	0.84	>150	$2.37^{+0.04}_{-0.09}$	>0.05	92^{+17}_{-13}	XMM/BAT	1,5
Mrk 841	0.036	8.5 ± 0.7	10	0.56	>597	$2.26^{+0.10}_{-0.09}$	>0.20	10^{+40}_{-8}	XMM/BAT	19

F_x is the 0.1–200 keV X-ray flux in 10^{-10} erg cm^{-2} s^{-1}.
[b]Reverberation results summarized on Misty Bentz's website (http://www.astro.gsu.edu/AGNmass/).
References: 1: Denney et al. (2010), 2: Baskin & Laor (2005), 3: Denney et al. (2009), 4: Winter et al. (2009), 5: Peterson et al. (2004), 6: Bentz et al. (2006), 7: Metzroth, Onken & Peterson (2006), 8: Bentz et al. (2009), 9: Bentz et al. (2010), 10: Emmanoulopoulos et al. (2014), 11: Uttley & McHardy (2005), 12: Barth et al. (2011), 13: Bian & Gu (2007), 14: Peterson et al. (2005), 15: Denney et al. (2006), 16: Barth et al. (2013), 17: Graham (2008), 18: Pancoast et al. (2014), 19: Middleton et al. (2007).
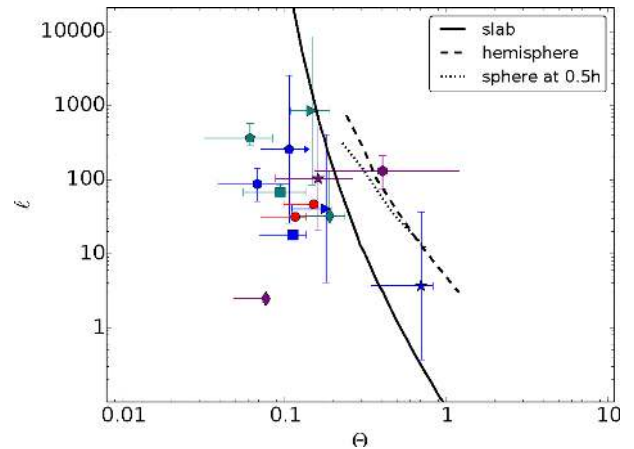
Table 5. Microlensing results on the coronae of AGN from *Chandra* observations. The references to the individual works are given in the right-most column.

Source	z	$\log(r_{co})$ (cm)	L [0.2–50 keV] (10^{-10} erg s^{-1})	E_{cut} (keV)	Θ	ℓ	References
QJ0158−4325	1.29	14.3	5.09E44	18	>0.02	>69	Chen et al. (2012); Morgan et al. (2012)
HE 0435−1223	1.69	14.8	5.03E44	22	>0.02	>22	Chen et al. (2012); Blackburne et al. (2014a)
SDSS J0924+0219	15	4.58	2.24E44	19	>0.02	>6	Chen et al. (2012); MacLeod et al. (2015)
HE 1104−1805	2.32	15.33	15.6E44	23	>0.02	>20	Chen et al. (2012); Blackburne et al. (2014b)
Q2237+0305	1.69	15.46	7.39E44	19	>0.02	>7	Chen et al. (2012); Mosquera et al. (2013)
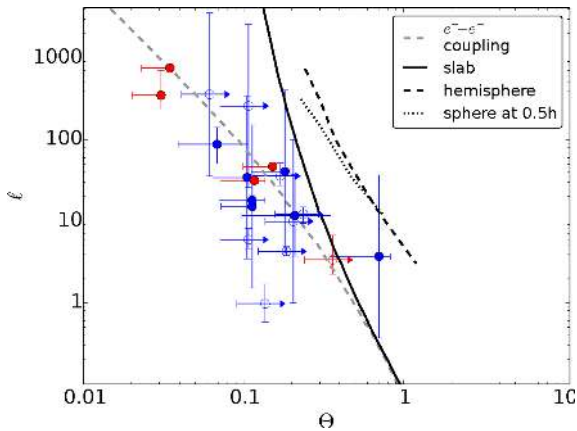
Figure 2. $\Theta - \ell$ distribution for *NuSTAR* observed AGN (blue points) and BHB (red points). The e–e coupling line from GHF is included. Pair lines from Stern et al. (1995) are shown. The slab line has been extrapolated slightly to higher ℓ.
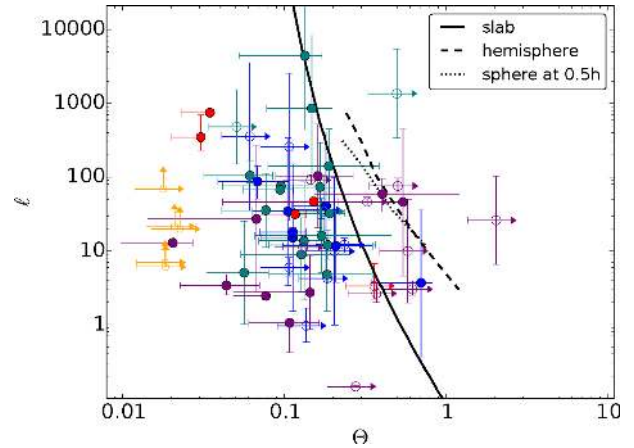
Figure 4. All measurements including Integral (teal), *Swift*-BAT (magenta) and gravitational lensed objects (yellow).

Figure 3. COMPPS (black) versus exponentially cutoff power law (red). See text for details.

Figure 5. Distribution of objects which have more measurements of ℓ and Θ from different instruments. The two red points are the two states of Cyg X-1.

the *NuSTAR* data on NGC 5506. The exponential cutoff energy is measured at 720^{+130}_{-190} keV whereas the COMPPS model (Poutanen et al. 1996) gives a temperature of 270 keV. Matt et al. (2015) also remind us of the comment by Gilli, Comastri & Hasinger (2007) that the mean value of E_{cut} for AGN must lie below 300 keV, in order not to saturate the X-ray Background at 100 keV. Objects such as NGC 5506 must be exceptional rather than the norm.

The results including the CAT2 sample are plotted in Fig. 4. As mentioned already these generally encompass cruder spectral modelling than used for the *NuSTAR* data, and the total exposures were each accumulated over several years. The sources generally concentrate around similar values to those measured with *NuSTAR*,

although there are a few outliers at high temperature. The most extreme one with $\Theta \sim 2$ is NGC 4388, a Seyfert 2 galaxy in the Virgo cluster. The measurement is with the *Swift*-BAT, the upper energy of which is 200 keV so could be suffering from the effect shown in Fig. 4. Objects where there are two pairs of $\Theta - \ell$ values are plotted in Fig. 5.

The distribution of high-energy cutoff values from the various samples is shown in Fig. 6. To make use of all measurements including lower limits, we calculate the histograms and errors using Monte Carlo simulations. For each realization of the histogram we draw for each cutoff constraint a cutoff value within its error range
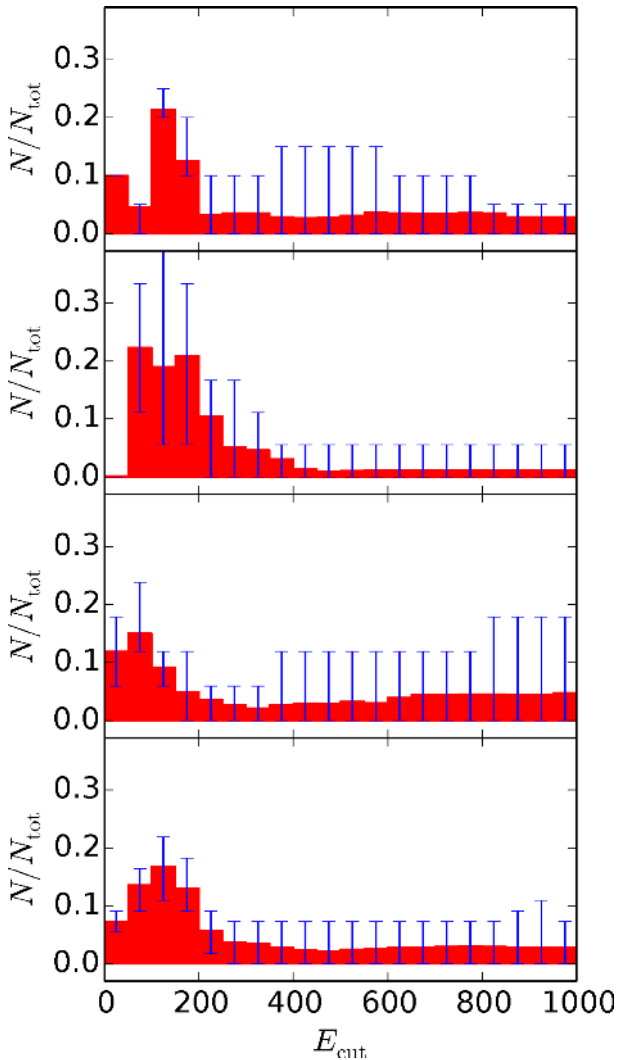
Figure 6. Histograms of Θ estimates: from top to bottom, *NuSTAR* sample (see text), Integral Malizia et al. (2014), *Swift*-BAT Vasudevan et al. (2013), entire sample.

(for the lower limits, 1000 keV is assumed to be the upper limit.) The histograms show clear peaks in the range of 100–150 keV.

5 DISCUSSION

We find (Fig. 2) that the X-ray coronae measured by *NuSTAR* have ℓ ranging from 1 to 1000 with most lying between 10 and 100, and Θ ranging from 0.03 to 0.8, with most between 0.07 and 0.3. This places many sources against the pair runaway line for slab geometry. Given the remaining uncertainties in spectral modelling and size estimates it is plausible that many of the sources track close to that line. The clustering of sources in the $\Theta - \ell$ plane argues for a general physical reason, such as the pair line, attracting or constraining them to that region.

Many of the coronae lie in the region where General Relativistic effects such as gravitational redshift and light-bending are important. To see one change produced by the first effect, the temperatures have been corrected for gravitational redshift z in Fig. 7. The points now lie closer to the pair line for a slab but several still lie at a significantly lower value of Θ. GR will also affect our estimates of ℓ through the effects on L ($(1 + z)^{(3 + \alpha)}$ from Liouville's theorem) and
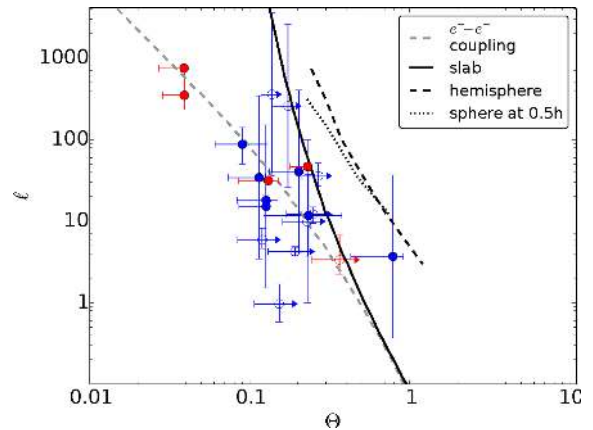

Figure 7. *NuSTAR* $\Theta - \ell$ distribution corrected for gravitational redshift.

R (which depends on the method by which this has been inferred). Light bending, in which the strong gravity bends radiation from the corona down towards the disc, requires another correction which is inclination dependent. The net effect is to boost the intrinsic values of ℓ by factors of around 2–10 above the observed estimates. As there is more uncertainty in these corrections we merely note that the estimates of ℓ should be seen as lower limits.

The coronal emission is likely anisotropic when the corona is close to the centre of the disc with factors such as spin and inclination affecting appearance. Wilkins & Fabian (2011) have used the emissivity profile of the iron line in several AGN to deduce the coronal illumination of the disc and thus indirectly constrain the size of the corona. In several cases the bulk of the coronal emission is tightly limited to a compact region above the centre of the disc, with radius r less than the height of the corona h, i.e. $r < h$, but with some emission originating from larger radii at the same height.

The geometrical considerations in the Stern et al. (1995) models mainly affect the ratio of soft photon to electron heating powers in the corona. The effects of light bending on the incidence of soft blackbody disc emission on the corona and the twisting of magnetic fields from the disc can modify the relevance of those geometries to the strong gravity regime above the centre of the accretion disc. As seen from the corona, the disc will appear to cover most of the Sky, possibly intensifying the effects of Compton cooling and moving the pair line to lower Θ.

Another possible reason for the offset in Θ values from the pair line is our assumption that the corona is homogeneous and single temperature. Instead, the corona may be very dynamic with heating localized and highly intermittent in space and time. This could produce a range of temperatures in the corona, all limited by the pair threshold, but with the mean at a lower value due to Compton cooling. Since pairs are produced by the high-energy tail of the particle and photon energy distributions, only a small dispersion in temperatures can have a large effect. This would imply that deeper observations[2] should reveal a high-energy tail to the spectra above that expected from single-temperature Comptonization.

A variant of this possibility occurs if the protons in the corona are much hotter and the source of some of the electron heating, then proton–electron coupling, may create a high-energy tail which produces pairs at a lower 'temperature' than expected for a strict

---

[2] We note that the BHB GRS 1915+105 (Miller et al. 2013), GRS 1739−278 (Miller et al. 2015) and Cyg X-1 (Parker et al. 2015) already show signs of possible hard tails in their spectral residuals.
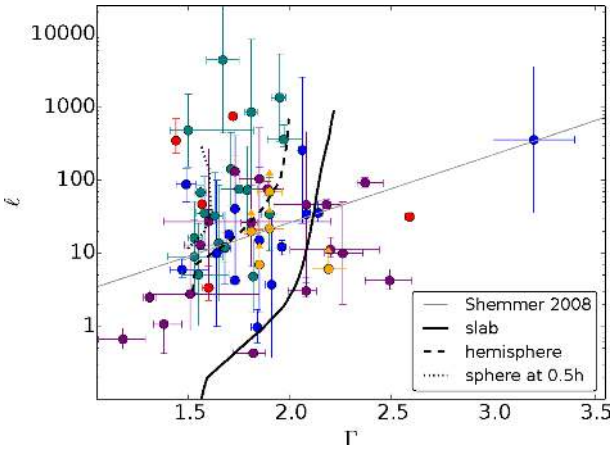
Figure 8. Distribution of ℓ plotted versus photon indices Γ. Lines from the Stern et al. (1995) models (see also Svensson 1996) are indicated.

Maxwellian distribution. More generally, such effects will apply to sources above the electron–electron coupling line. Indeed, the parts of the corona of where heating is most intense may exceed this constraint. The electron distribution may not then be Maxwellian. This need not greatly affect the Comptonized spectrum, which will resemble that from a thermal electron population with the same mean value of $(\gamma^2 - 1)$, where γ is the electron Lorentz factor (GHF; see also Nayakshin & Melia 1998).

Many sources are (marginally) above the electron–electron coupling line and all are above the electron–proton line. This emphasizes the longstanding problems of the heating and thermalization process (Guilbert, Fabian & Stepney 1982; Svensson 1999; Merloni & Fabian 2001; GHF). All sources have a cooling time less than the light crossing time so the energy must be present there in some other form. Since protons cannot supply the energy to the electrons fast enough, due to the long coupling time (Fig. 1), we presume that it must be in terms of magnetic field. As indicated many times before (e.g. Merloni & Fabian 2001), the corona must be magnetically dominated. An underlying strong magnetic field means that the synchrotron boiler dominates the energy exchange between low-energy electrons and the photon field (Ghisellini, Guilbert & Svensson 1988; Ghisellini, Haardt & Svensson 1998; Belmont, Malzac & Marcowith 2008; Veledina, Vurm & Poutanen 2011). Taking these issues further is beyond the scope of this paper.

We note that all the sources that we have examined are above the Eddington limit for pairs. We have assumed in all cases that the source is static. Magnetic fields are presumably responsible for holding the bulk of the source together, although that does not exclude a pair wind escaping from part of the source (e.g. Beloborodov 1999) or being accelerated into a jet (Henri & Pelletier 1991; Mościbrodska et al. 2011). The pair limit may be avoided if the emission region is part of a relativistic outflow, such as a Gamma-ray burst (e.g. Piran 2004). Note that no distinct annihilation line should be observable from a thermal pair plasma (Zdziarski 1984).

The modelling by Stern et al. (1995) and others indicates that the Thomson depth of the scattering region should be less than unity. Most of the coronal particles can be pairs. Pair balance together with the geometry dictates the expected spectra shape of the coronal continuum. The observed photon index Γ is plotted against ℓ in Fig. 8. There is some agreement with the Stern et al. (1995) model predictions in the $\Gamma - \ell$ plane. We also include a line from the work of Shemmer et al. (2008) who find an observational correlation (with much scatter) between Eddington fraction, L/L_{Edd}, and photon index

Γ. For a given coronal size R, this relates to ℓ through equation (2). The position of this line in the y-axis thus depends on R.

We stress that the pair limit to the temperature of luminous, static, compact regions cannot be avoided. It explains the rough uniformity and trend in cutoff energy (higher values of E_{cut} occur at lower values of ℓ in Fig. 2) that is emerging from *NuSTAR* observations of AGN and BHB. Temperatures close to the pair line at $\Theta \sim 0.1$–0.25 are expected when such high powers are dissipated in the physically compact regions found immediately around accreting black holes. Further detailed computations are required to make more precise predictions for sources in the observed $\Theta - \ell$ plane, taking into account the effects of heating, thermalization, inhomogeneities, geometry and light bending. Future hard X-ray observations with NuSTAR and ASTRO-H will map the $\Theta - \ell$ plane in more detail and, with improved theoretical models, lead to a deeper understanding of the central engine of AGN, the most luminous persistent sources in the Universe.

REFERENCES

Ballantyne D. R. et al., 2014, ApJ, 794, 62
Baloković M. et al., 2015, ApJ, 800, 62
Barth A. J. et al., 2011, ApJ, 743, L4
Barth A. J. et al., 2013, ApJ, 769, 128
Baskin A., Laor A., 2005, MNRAS, 356, 1029
Beckmann V. et al., 2009, A&A, 505, 26
Belmont R., Malzac J., Marcowith A., 2008, A&A, 491, 617
Beloborodov A. M., 1999, ApJ, 510, L123
Bentz M. C. et al., 2006, ApJ, 651, 775
Bentz M. C., Peterson B. M., Netzer H., Pogge R. W., Vestergaard M., 2009, ApJ, 697, 160
Bentz M. C. et al., 2010, ApJ, 716, 993
Bian W., Gu Q., 2007, ApJ, 657, 159
Bian W., Zhao Y., 2003, MNRAS, 343, 164
Bianchi S., Guainazzi M., Matt G., Fonseca Bonilla N., Ponti G., 2009, A&A, 495, 421
Bisnovatyi-Kogan G. S., Zeldovich Ya. B., Sunyaev R. A., 1971, SvA, 15, 17
Blackburne J. A., Kochanek C. S., Chen B., Dai X., Chartas G., 2014a, ApJ, 789, 125
Blackburne J. A., Kochanek C. S., Chen B., Dai X., Chartas G., 2014b, ApJ, 798, 95
Blank D. L., Harnett J. I., Jones P. A., 2005, MNRAS, 356, 734
Brenneman L. W. et al., 2014, ApJ, 788, 61
Cackett E. M., Zoghbi A., Reynolds C., Fabian A. C., Kara E., Uttley P., Wilkins D. R., 2014, MNRAS, 438, 2980
Cavaliere A., Morrison P., 1980, ApJ, 238, L63
Chen B., Dai X., Kochanek C. S., Chartas G., Blackburne J. A., Morgan C. W., 2012, ApJ, 755, 24
Church M. J., Balucinska-Church M., 2004, MNRAS, 348, 955
Coppi P. S., 1999, in Poutanen J., Svensson R., eds, ASP Conf. Ser., Vol. 161, High Energy Processes in Accreting Black Holes. Astron. Soc. Pac., San Francisco, p. 375
De Marco B., Ponti G., Uttley P., Cappi M., Dadina M., Fabian A. C., Miniutti G., 2011, MNRAS, 417, L98

Dennerl K., Greiner J., 1996, IAU Circ., 6426
Denney K. D. et al., 2006, ApJ, 653, 152
Denney K. D. et al., 2009, ApJ, 702, 1353
Denney K. D. et al., 2010, ApJ, 721, 715
Done C., Fabian A. C., 1989, MNRAS, 240, 81
Dove J. B., Wilms J., Maisack M., Begelman M. C., 1997, ApJ, 487, 759
Emmanoulopoulos D., Papadakis I. E., Doviak M., McHardy I. M., 2014, MNRAS, 439, 3931
Fabian A. C., 1994, ApJS, 92, 555
Fabian A., 2012, ARA&A, 50, 455
Fabian A. C. et al., 2009, Nature, 459, 540
Fuerst F., Al. E., 2015, ApJ, in press
Ghisellini G., Guilbert P. W., Svensson R., 1988, ApJ, 334, L5
Ghisellini G., Haardt F., Fabian A. C., 1993, MNRAS, 263 (GHF)
Ghisellini G., Haardt F., Svensson R., 1998, MNRAS, 297, 348
Gilli R., Comastri A., Hasinger G., 2007, A&A, 463, 79
Graham A. W., 2008, Publ. Astron. Soc. Aust., 25, 167
Greiner J., Dennerl K., Predehl P., 1996, A&A, 314, 21
Grier C. J. et al., 2012, ApJ, 744, L4
Grier C. J. et al., 2013, ApJ, 773, 90
Guainazzi M., Bianchi S., Matt G., Dadina M., Kaastra J., Malzac J., Risaliti G., 2010, MNRAS, 406, 2013
Guilbert P. W., Fabian A. C., Stepney S., 1982, MNRAS, 199, 19
Guilbert P., Fabian A., Rees M., 1983, MNRAS, 205, 593 (GFR)
Haardt F., Maraschi L., 1993, ApJ, 413, 507
Henri G., Pelletier G., 1991, ApJ, 383, L7
Hicks E. K. S., Malkan M. A., 2008, ApJS, 174, 31
Kara E., Cackett E. M., Fabian A. C., Reynolds C., Uttley P., 2013, MNRAS, 439, L26
Kara E. et al., 2015, MNRAS, 449, 234
MacLeod C. L. et al., 2015, preprint (arXiv:1501.07533)
Malizia A. et al., 2008, MNRAS, 389, 1360
Malizia A., Molina M., Bassani L., Stephen J. B., Bazzano A., Ubertini P., Bird A. J., 2014, ApJ, 782, L25
Marinucci A. et al., 2014a, MNRAS, 447, 160
Marinucci A. et al., 2014b, MNRAS, 440, 2347
Marinucci A. et al., 2014c, ApJ, 787, 83
Masetti N. et al., 2006, A&A, 459, 21
Masetti N. et al., 2009, A&A, 495, 121
Matt G. et al., 2014, MNRAS, 439, 3016
Matt G. et al., 2015, MNRAS, 447, 3029
Merloni A., Fabian A. C., 2001, MNRAS, 321, 549
Merloni A., Fabian A. C., 2003, MNRAS, 342, 951
Metzroth K. G., Onken C. A., Peterson B. M., 2006, ApJ, 647, 901
Middleton M., Done C., Schurch N., 2007, MNRAS, 383, 1501
Miller J. M. et al., 2013, ApJ, 775, L45
Miller J. M. et al., 2015, ApJ, 799, L6
Moran E. C., Barth A. J., Eracleous M., Kay L. E., 2007, ApJ, 668, L31
Morgan C. W. et al., 2012, ApJ, 756, 52
Mościbrodska M., Gammie C. F., Dolence J. C., Shiokawa H., 2011, ApJ, 735, 9
Mosquera A. M., Kochanek C. S., Chen B., Dai X., Blackburne J. A., Chartas G., 2013, ApJ, 769, 53
Nayakshin S., Melia F., 1998, ApJS, 114, 269
Orosz J. A., McClintock J. E., Aufdenberg J. P., Remillard R. A., Reid M. J., Narayan R., Gou L., 2011, ApJ, 742, 84
Pancoast A., Brewer B. J., Treu T., Park D., Barth A. J., Bentz M. C., Woo J.-H., 2014, MNRAS, 445, 3073
Parker M. L. et al., 2014, MNRAS, 443, 1723
Parker M. L. et al., 2015, ApJ, in press
Peterson B. M. et al., 2004, ApJ, 613, 682
Peterson B. M. et al., 2005, ApJ, 632, 799
Petrucci P. O. et al., 2001, ApJ, 556, 716
Pietrini P., Krolik J. H., 1995, ApJ, 447, 526
Piran T., 2004, Rev. Mod. Phys., 76, 1143
Ponti G., Papadakis I., Bianchi S., Guainazzi M., Matt G., Uttley P., Bonilla N. F., 2012, A&A, 542, A83
Poutanen J., Nagendra K. N., Svensson R., 1996, MNRAS, 283, 892
Reid M. J., McClintock J. E., Narayan R., Gou L., Remillard R. A., Orosz J. A., 2011, ApJ, 742, 83
Reis R. C., Miller J. M., 2013, ApJ, 769, L7
Reynolds C. S. et al., 2015, ApJ, submitted
Risaliti G., Nardini E., Elvis M., Brenneman L., Salvati M., 2011, MNRAS, 417, 178
Sanfrutos M., Miniutti G., Agis-Gonzalez B., Fabian A. C., Miller J. M., Panessa F., Zoghbi A., 2013, MNRAS, 436, 1588
Shemmer O., Brandt W. N., Netzer H., Maiolino R., Kaspi S., 2008, ApJ, 682, 81
Steeghs D., McClintock J. E., Parsons S. G., Reid M. J., Littlefair S., Dhillon V. S., 2013, ApJ, 768, 185
Stern B. E., Poutanen J., Svensson R., Sikora M., Begelman M. C., 1995, ApJ, 449, 13
Svensson R., 1982, ApJ, 258, 335
Svensson R., 1984, MNRAS, 209, 175
Svensson R., 1996, A&AS, 120, 475
Svensson R., 1999, ASP Conf. Ser. Vol. 161, High Energy Processes in Accreting Black Holes, Astron. Soc. Pac., San Francisco, p. 361
Tadhunter C., Marconi A., Axon D., Wills K., Robinson T. G., Jackson N., 2003, MNRAS, 342, 861
Tomsick J. A. et al., 2014, ApJ, 780, 78
Ursini F. et al., 2015a, A&A, 577, A38
Ursini F. et al., 2015b, MNRAS, submitted
Uttley P., McHardy I. M., 2005, MNRAS, 363, 586
Uttley P., Cackett E. M., Fabian A. C., Kara E., Wilkins D. R., 2014, A&AR, 22, 72
Vaiana G. S., Rosner R., 1978, ARA&A, 16, 393
Vasudevan R. V., Brandt W. N., Mushotzky R. F., Winter L. M., Baumgartner W. H., Shimizu T. T., Schneider D. P., Nousek J., 2013, ApJ, 763, 111
Veledina A., Vurm I., Poutanen J., 2011, MNRAS, 414, 3330
Wilkins D. R., Fabian A. C., 2011, MNRAS, 414, 1269
Winter L. M., Mushotzky R. F., Reynolds C. S., Tueller J., 2009, ApJ, 690, 1322
Woo J., Urry C. M., 2002, ApJ, 579, 530
Zdziarski A. A., 1984, ApJ, 283, 842
Zdziarski A. A., 1985, ApJ, 289, 514
Zdziarski A. A., Lubinski P., Gilfanov M., Revnivtsev M., 2003, MNRAS, 342, 355
Zdziarski A. A., GierliÅski M., MikoÅajewska J., WardziÅski G., Smith D. M., Alan Harmon B., Kitamoto S., 2004, MNRAS, 351, 791
Zoghbi A. et al., 2014, ApJ, 789, 56

This paper has been typeset from a T<small>E</small>X/L<small>A</small>T<small>E</small>X file prepared by the author.